Distribution and evolution of chorus waves modeled by a neural network: the importance of imbalanced regression

Xiangning Chu[1], Jacob Bortnik[2], Wen Li[3], Xiao-Chen Shen[3], Qianli Ma[2,3], Donglai Ma[2], David Malaspina[1], and Sheng Huang[3]

[1] Laboratory for Atmospheric and Space Physics, University of Colorado Boulder, Boulder, Colorado, USA

[2] Department of Atmospheric and Oceanic Sciences, University of California, Los Angeles, California, USA

[3] Center for Space Physics, Boston University, Boston, Massachusetts, USA

Corresponding author: Xiangning Chu (chuxiangning@gmail.com)

Key Points:

- A neural network model of lower-band chorus wave amplitude is developed using imbalanced regression
- For the first time, a chorus model can predict the large amplitude of strong chorus waves

- Chorus' evolution is consistent with electron injection drift paths, peak equatorial amplitude near midnight, and off-equator peaks at noon

Abstract

Whistler-mode chorus waves play an essential role in the acceleration and loss of energetic electrons in the Earth's inner magnetosphere, with the more intense waves producing the most dramatic effects. However, it is challenging to predict the amplitude of strong chorus waves due to the imbalanced nature of the dataset, i.e., there are many more non-chorus data points than strong chorus waves. Thus, traditional models usually underestimate chorus wave amplitudes significantly during active times. Using an imbalanced regressive (IR) method, we develop a neural network model of lower-band (LB) chorus waves using 7-year observations from the EMFISIS instrument onboard Van Allen Probes. The feature selection process suggests that the auroral electrojet index alone captures most of the variations of chorus waves. The large amplitude of strong chorus waves can be predicted for the first time. Furthermore, our model shows that the equatorial LB chorus's spatiotemporal evolution is similar to the drift path of substorm-injected electrons. We also show that the chorus waves have a peak amplitude at the equator in the source MLT near midnight, but toward noon, there is a local minimum in amplitude at the equator with two off-equator amplitude peaks in both hemispheres, likely caused by the bifurcated drift paths of substorm injections on the dayside. The IR-based chorus model will improve radiation belt prediction by providing chorus wave distributions, especially storm-time strong chorus. Since data imbalance is ubiquitous and inherent in space physics and other physical systems, imbalanced regressive methods deserve more attention in space physics.

Plain Language Summary

Whistler-mode chorus waves are essential in accelerating radiation belt electrons. However, predicting the amplitude of strong chorus waves is difficult because of their imbalanced nature.

In other words, there are many more observations of no-chorus waves than strong chorus waves. A consequence is that these no-chorus wave data dominate traditional models, so these models usually predict values that are too small for strong waves. Using an imbalanced regressive method, we developed a machine learning (ML) model of lower-band chorus wave amplitude. For the first time, the ML-chorus model can predict the amplitude of strong chorus waves. The ML-chorus model shows the evolution of the chorus wave at the equator, similar to the drift path of injected electrons, which brings electron anisotropy that generates chorus waves. The ML-chorus model shows that the chorus waves are stronger at the equator near midnight, the source region of plasma injection. Away from midnight, the chorus waves have an equatorial minimum instead. Our chorus model will improve the forecast of the radiation belt environment by providing chorus wave distributions, especially large-amplitude strong chorus during geomagnetic storms. Because data imbalance is commonly seen in space physics and other physical systems, imbalanced regressive methods require more attention.

1 Introduction

1.1 Radiation belt dynamics and chorus waves

The Earth's outer Van Allen radiation belt consists of trapped energetic electrons (~MeV), the dynamics of which result from a delicate and competitive balance between acceleration, loss, and transport processes (Baker et al., 2013, 2014a, 2014b; Lee et al., 2013; Li et al., 2013; Ma et al., 2018; Meredith et al., 2003; Ni et al., 2013; Reeves et al., 1998, 2003; Thorne et al., 2013a, 2013b). Local acceleration driven by whistler-mode chorus waves plays an essential role in accelerating seed electrons to relativistic and ultra-relativistic energies (Horne and Thorne, 1998; Summers et al., 2002; Thorne et al., 2013b), and pitch angle scattering of plasma sheet electrons by chorus leads to electron precipitation into the upper atmosphere to produce diffuse aurora (Ni et al., 2008, 2016; Thorne et al., 2010) and pulsating aurora (Kasahara et al., 2018; Nishimura et al., 2010).

Whistler-mode chorus waves are intense electromagnetic waves typically showing discrete elements that are excited naturally in the low-density region outside the plasmapause due to a cyclotron instability of anisotropic energetic electrons (Burtis and Helliwell, 1976; Meredith et al., 2001, 2003a; Santolik et al., 2003; Tsurutani and Smith, 1974). These anisotropic electrons are believed to form due to electrons injected from the plasma sheet into the inner magnetosphere, conserving their first two adiabatic invariants (e.g., Katoh and Omura, 2007; Li et al., 2010; Nunn, 1974). However, validating this theory using observations is not trivial since it requires multi-point in-situ observations of the chorus waves and the electron velocity distributions, with the observations taken such that they follow the electron drift path of the injections. Chorus waves typically occur in the frequency range of 0.1–0.8 f_{ce} (the equatorial electron cyclotron frequency) and are organized into two distinct bands (lower and upper bands) with a gap near 0.5 f_{ce} (Li et al., 2019; Meredith et al., 2012; Santolík et al., 2003; Tsurutani and Smith, 1977). Previous studies have shown that nightside chorus waves are peaked near the equator, whereas dayside chorus waves can extend to higher magnetic latitudes (MLAT) (e.g., Agapitov et al., 2013, 2015; Bortnik et al., 2007; Bortnik and Thorne, 2007; Bunch et al., 2011; Li et al., 2009). In addition, the chorus wave is believed to be one of the origins of plasmaspheric hiss (Agapitov et al., 2018; Bortnik et al., 2008, 2009; Chen et al., 2009; Hartley et al., 2019; Meredith et al., 2013b).

There have been many studies on modeling the properties of chorus waves. The average wave amplitude is generally statistically modeled as a function of spatial location (L shell, MLT, and MLAT), and parameters used to categorize the chorus wave amplitude include solar wind parameters, geomagnetic indices, or a combination of these parameters (Aryan et al., 2014, 2016, 2020; Agapitov et al., 2015, 2018; Li et al., 2009, 2013, 2016; Meredith et al., 2012, 2018, 2020; Wang et al., 2019). Chorus waves have also been modeled using neural networks (Guo et al., 2022; Kim et al., 2013; Bortnik et al., 2018), performing better in errors than the statistically averaged models. However, these models generally fail to predict the correct intensity of strong chorus waves due to the highly imbalanced nature of the chorus database, which is discussed below.

1.2 Imbalanced regression and shortcomings of standard regression models

Data imbalance is a ubiquitous problem inherent in the real world. Real-world data sets are usually not uniformly distributed and generally exhibit skewed distributions with a long tail, where specific values (typical of little interest) have much more data samples than the other ranges with very few samples (but are of the most interest). Imbalanced datasets have been an essential problem in machine learning (ML) (Buda et al., 2018; Liu et al., 2019). The challenge of imbalanced data has been discussed and investigated in many studies in the field of machine learning (Cao et al., 2019; Cui et al., 2019; Huang et al., 2019; Liu et al., 2019; Tang et al., 2020; Yang et al., 2021). Nevertheless, most existing studies for learning from imbalanced data focus on classification problems, i.e., targeted parameters with categorical values. However, many real-world tasks are inherently regression problems, i.e., the target values are continuous across the domain. For an example of regression, in the field of vision applications, a popular large-scale image database is called IMDB-WIKI (Rothe et al., 2018). It is used to estimate the age of different people based on their visual appearance. The target parameter, people's age, is a continuous target and highly imbalanced in the IMDB-WIKI database. The challenge of imbalanced data also exists in medical applications. The target parameters of heart rate, blood pressure, and oxygen saturation are continuous, and their distributions are usually skewed across the patient populations, with the anomalous, elevated values (that are of most interest to patients) occurring for only a small fraction of the data samples.

In space physics, most of the physical parameters, if not all, are imbalanced datasets. For instance, the most popular geomagnetic indices, the auroral electrojet indices (*AE*, *AU*, and *AL*), the ring current index *Dst*, and the *Kp* index are skewed toward low values due to the large number of observations taken during quiet times rather than active times. The relativistic electron fluxes in the Earth's radiation belt or measured at geosynchronous orbit are also skewed toward the quiet time averages (e.g., Figure 1 in Baker et al. [2019]). Solar images, which are used to predict solar flare events, Coronal Mass Ejections (CME), and solar wind speed, also capture much quieter images far more often than solar irruptions [Al-Ghraibah et al., 2015; Nishizuka et al., 2021; Wan et al., 2021]. Therefore, imbalanced data sets are also ubiquitous in space physics.

Successful applications of statistical and ML-based regression models improved our understanding of the magnetospheric and ionospheric response to the solar wind drivers (see summary in Camporeale (2019) and references therein). However, it was brought to scientists' attention that the regression models provide poor predictions during active times (e.g., Chakraborty et al., 2020; Lazzús et al., 2017; Tan et al., 2018), especially during large to extreme events due to the too-often-too-quiet problem (Camporeale, 2019). The traditional method of regression, either statistical or ML-based, is fairly heuristic and suffers from the shortcomings of imbalanced data. For instance, the error metrics, mean squared errors (MSE), are commonly used in previous studies (e.g., see discussion in [Temerin and Li, 2002]). In the case of imbalanced data, the MSE is dominated by many quiet-time observations. To maintain a zero mean of the errors, the large volume of quiet time data is usually slightly overestimated toward higher values. On the other hand, the small volume of large values during active times (or large-to-extreme events) is usually underestimated significantly toward lower values. Therefore, it usually leads to unrealistic biases when predicting quiet time and active values.

Due to the imbalanced nature of the chorus waves, traditional statistical models cannot reproduce the time-dependent variations of chorus waves, especially the strong wave amplitude (see discussion in Guo et al. [2021]). Therefore, for the first time, we developed a neural network model for the lower-band (LB) chorus wave amplitude using an imbalanced regressive (IR) method, which can accurately predict both background noise and large wave amplitudes. Furthermore, the model provides time-dependent and global variations of chorus wave amplitude and is used to study the evolution of the LB chorus waves during a typical event.

2 Data Description

2.1 Database

In this study, chorus waves in the Earth's inner magnetosphere are modeled using an imbalanced regressive (IR) neural network model. The primary dataset consists of the wave amplitude of the lower band (LB) chorus waves taken from Van Allen Probes (RBSP) and geomagnetic indices from the OMNI database and SuperMAG.

NASA's Van Allen Probes spacecraft consists of two identically equipped satellites in near-equatorial orbits with an apogee of ~6 R_E and an orbit period of ~9 hours (Mauk et al., 2013). The two spacecraft have almost identical orbits with varying spacecraft separation along the track. The plasma density is obtained using the upper hybrid resonance frequency identified from the High-Frequency Receiver (HFR) on Electric and Magnetic Field Instrument Suite and Integrated Science (EMFISIS) (Kletzing et al., 2013; Kurth et al., 2015). Chorus waves are analyzed using measurements from the Waveform Receiver (WFR) on the EMFISIS wave instrument (Kletzing et al., 2013). The LB chorus waves are identified using the following criteria: (1) they occur outside the plasmapause, (2) within the frequency range of 0.05-0.5 f_{ce}, (3) they have planarity > 0.6, and (4) ellipticity > 0.7 (see detailed description in Li et al. (2016) and Shen et al., (2019)). The plasmasphere could be identified using the intensity of the electron cyclotron harmonic (ECH) waves (Meredith et al., 2004), and we follow the procedure by Shen et al. (2019) to find the measurements outside the plasmapause along the Van Allen Probes orbit. Using the above criteria, the wave amplitude of the LB chorus waves is obtained along Van Allen Probes' trajectory from January 1, 2013, to the end of the mission (August 1, 2019 for RBSP-A and July 16, 2019 for RBSP-B). For observations with no chorus waves, the wave amplitude is filled by 0.1 pT as the lower threshold. Due to the satellite procession, the satellite measurements covered all MLT sectors more than three times throughout the mission lifetime. The dataset has more than 66 million data samples every ~6 seconds. This study reduces the temporal resolution to 5 min averages while conserving the mean wave power (Bw^2), which results in ~1.4 million data samples.

The solar wind conditions and geomagnetic indices are obtained from the OMNI dataset (https://omniweb.gsfc.nasa.gov/) (Papitashvili et al., 2020) and SuperMAG (https://supermag.jhuapl.edu/) (Gjerloev et al., 2010), which are used as potential input parameters to the neural network model.

2.2 Data distribution of chorus waves

Figure 1 shows the statistical distribution of the dataset with respect to its locations and several important factors. Figure 1a shows that the observations of Van Allen Probes are within the L shell range of 2.0 and 7.0 and |MLAT|<20°. The majority of observations are taken between L~5.8 near the apogee of Van Allen Probes, with more observations taken near the equator than at higher latitudes. Figure 1b shows that the observations are relatively evenly distributed relative to MLTs. Figures 1c and 1d are in the same format as Figures 1a and 1b when Bw>5*pT*. Note that these samples (Bw>5*pT*) are mostly located at high L shells. Figure 1e shows that the dataset is highly imbalanced with respect to the chorus wave amplitude, where quiet-time observations dominate the whole dataset. About 90.0% of the observations are below 3.5 *pT*, and *94.4%* of the data are below 10.0 *pT*. Figure 1f shows that chorus waves are well organized by plasma density. Chorus waves are usually observed at low-density regions *(<100* cm^{-3}) outside the plasmapause, as expected [Hartley et al., 2022; Malaspina et al., 2016, 2018, 2020, 2021]. The statistical analysis above provides important information regarding the development of the neural network model, which will be discussed below.

3 Methodology

3.1 Model description

In this study, an LB chorus wave model is developed using a feedforward neural network following the workflow described by Chu et al. (2021). The neural network's architecture for the chorus wave model is similar to that used in previous studies, which successfully modeled global dynamic distributions of plasma density and electron and ion fluxes (Chu et al., 2017a, 2017b, 2021). It consists of a linear input layer, three hidden layers with a sigmoid activation function, each followed by a batch normalization layer, and a linear output layer. The input parameters include the location of the measurements (i.e., L shell, MLT, and MLAT), the in-situ electron density, and the time series of the solar wind parameters and geomagnetic indices from the OMNI and SuperMAG dataset, which is discussed in greater detail below. The target parameter, also referred to as the model output, is the base ten logarithms of the wave amplitude of the LB chorus waves $log_{10}(B_w)$. The model inputs and output are normalized using each parameter's mean and standard deviation before training and scaled back when making predictions.

It is essential to perform imbalanced regression since the dataset of chorus waves is highly imbalanced, having more quiet-time background samples than the active-time, large-amplitude chorus samples of interest. The chorus wave dataset is categorized by amplitude: quiet background ($Bw<2\ pT$), weak ($2\ pT<Bw<5\ pT$), and strong ($Bw>5\ pT$). The integrated wave amplitude of $Bw\sim2\ pT$ is roughly the noise level of the EMFISIS instrument (Kletzing et al., 2013). Also, the amplitude of 2 pT is close to the local peak value in the histogram of the wave amplitude (Figure 1e), the elbow point from a power law, suggesting two distinct distributions. Thus, the quiet background values are chosen as $Bw<2\ pT$ and assigned a weight of 1.0. Another elbow point is found at $Bw\sim5\ pT$, shown as the slower decrease of sample number with increasing Bw at $Bw>5\ pT$ than that at $Bw<5\ pT$. Therefore, these weak chorus waves of $2\ pT<Bw<5\ pT$ are assigned a weight of 10. These strong chorus waves ($Bw>5\ pT$) are assigned a weight of 20. The weights for each category are chosen empirically based on a number of experiments when the data-model comparison is along the diagonal line, as shown in Figure 2. The data-model comparison pairs show different degrees of biases (offset from the diagonal line) in the range of different categories for different experiments, and we chose the experiment that yields minimal biases in all ranges. In addition, without proper weights, the model prediction exhibits a cutoff at large values around tens of pT for different experiments (see Figure 8 and

Section 5 for discussion), and we chose the experiment without the cutoff. The loss function is the weighted mean squared error (*WMSE*) of the $log_{10}(B_w)$.

$$WMSE = \frac{\sum_1^n w_i (Bw_{obs} - Bw_{model})^2}{n \sum_1^n w_i}$$

where w_i is the weight of each data sample. To minimize the loss function, the neural network model is trained using the Nesterov-accelerated Adaptive Moment Estimation (*Nadam*) optimizer (Dozat, 2016). To avoid data leakage, the whole dataset is split into daily segments. This 1-day period is much longer than the typical time scale (1 hour) of chorus wave dynamics, i.e., the substorm duration (~1 hour) (Chu et al., 2015) that is known to be the primary driver of chorus waves. Then, 60% of the 1-day segments are randomly selected as the training data, 20% as the validation set, and 20% as the test set. To avoid overfitting, we applied early stopping with 15 epochs, dropout layers after each hidden layer (Srivastava et al., 2014), and modified stratified five-fold cross-validation (Chu et al., 2021).

To make global and time-dependent reconstructions of chorus wave amplitude, the plasma density at every spatial location and time is required, but not available. Therefore, a pilot neural-network-based electron density model has been developed using a 1-min electron density obtained from EMFISIS, similar to our previous models (Bortnik et al., 2016; Chu et al., 2017a, b). This model provides global distributions of electron density that are used as the input to the chorus model. Since we have introduced the plasma density model in our past studies (Bortnik et al., 2016; Chu et al., 2017a, b), we do not elaborate on the details here.

3.2 Feature selection and hyperparameter optimization

We used the same feature selection and hyperparameter optimization (HPO) processes discussed in Chu et al. (2021). It is based on the strategy of sequentially adding the most informative predictors for the neural network model and assessing its performance (Kuhn et al., 2013). First, the locations of each measurement (*L* shell, MLT, and MLAT) are used as input. Second, the location plus the time series of one parameter from the OMNI and SuperMAG database are used as the only inputs. We used 1 min resolution of the indices for the preceding three hours and hourly averages for the preceding 24 hours, which are chosen empirically. We used a modified stratified five-fold cross-validation approach for the training process (https://scikit-learn.org/stable/modules/cross_validation.html). The input parameters include all the parameters in the OMNI dataset (https://omniweb.gsfc.nasa.gov/) and the geomagnetic indices from SuperMAG (SME/U/L/R). After looping through all the input parameters, the SME index (SuperMAG auroral index) yields the best performance among all input parameters. The SME index, the auroral electrojet indices reflective of the horizontal currents in the ionosphere, indicates the plasma injections from the magnetotail. This result is expected since the chorus waves are excited due to the electron anisotropy associated with plasma injections (Li et al., 2010). Third, we repeat the second step by adding the time series of another parameter from the

OMNI dataset as input. However, adding another parameter did not improve the model performance further (i.e., the error does not decrease).

The hyperparameters of the neural network model, including the number of neurons in each hidden layer and the dropout rates, are optimized using a Tree-structured Parzen estimator algorithm (Bergstra et al., 2011, 2013) implemented in Optuna (Akiba et al., 2019). We use a modified stratified 5-fold cross-validation, and the model yields the best performance on the validation dataset chosen. The final model has three hidden layers with 180, 184, and 43 neurons and dropout rates of 0.47, 0.22, and 0.20, respectively.

3.3 Model uncertainty

A second pilot model of the uncertainty of the chorus model was developed, following a similar protocol to our previous work (Camporeale et al., 2019). The uncertainty is defined as the absolute error between the observed and modeled LB chorus wave amplitude:

$$uncertainty = |\log_{10}(Bw_{obs}) - \log_{10}(Bw_{model})| = |\log_{10}\frac{Bw_{obs}}{Bw_{model}}|$$

The uncertainty model takes the same input as the chorus model (see section 3.1 for details) and predicts the absolute error of the predicted chorus wave amplitude $log_{10}(B_w)$, which is usually close to a Gaussian distribution, as shown in Figure 16 in Camporeale et al., (2019). Thus, the uncertainty denotes a relative error in the wave amplitude so that the ratios of Bw are symmetric both above and below 1 (Morley et al., 2018). Finally, both the chorus wave amplitude and its uncertainty can be provided by the two neural network models at any time and at any location, i.e., time-dependent uncertainties. An example of the modeled chorus wave amplitude and its uncertainty along the Van Allen Probe's trajectories are discussed in section 5 with Figure 5. The error bars represent the modeled chorus wave amplitudes plus and minus the modeled uncertainties.

4 Model performance

The correlation between the observed and modeled chorus wave amplitude $log_{10}(B_w)$ above the background level is shown in the four panels in Figure 2 for the whole dataset, as well as the training, validation, and test datasets separately. The probability density of occurrences in each bin is indicated by its color. The red dashed diagonal line ($y=x$) represents where the model predicts the wave amplitude perfectly, as expected. It should be noted that most observation-model pairs are distributed around the diagonal line. This result suggests that the neural network model reproduces the observations without much over- or under-estimation, regardless of the chorus amplitude $log_{10}(B_w)$. Particular attention has been given to these large values, which are also well-predicted. While this is intuitively correct and was relatively easy to obtain in previous models (e.g., plasma density in Bortnik et al., 2016; Chu et al., 2017a, b; electron fluxes in Chu et al., 2021; Ma et al., 2022), it has been challenging to achieve using highly imbalanced data such as the chorus wave amplitude. Traditional statistical models of chorus wave distribution, or any model based on an imbalanced dataset, are usually dominated by the frequently occurring background values. Furthermore, the traditional models usually minimize the mean squared error (MSE), with the assumption that each data point is equally important. As a result, these models tend to regress to the means of quiet-time values, and cannot predict large values in the long tail distribution. In the case of chorus waves, traditional statistical models usually underestimate the amplitude of large chorus waves. In this study, we show that an imbalanced regressive technique is essential during model development using imbalanced datasets, and our chorus model is the first model that can predict strong chorus waves.

Our chorus model can make accurate predictions of large chorus waves within a reasonable uncertainty. The weighted root mean square errors (WRMSE) are shown on the bottom right of the panels. The WRMSE on the test dataset is 0.53, which translates to an uncertainty of a factor of 3.3 (=$10^{0.53}$).

Figure 3 shows the probability density of the errors as a function of the L shell for the four datasets, for direct comparison to Figure 2. The error is defined as the difference between the logarithms of the observation and the model prediction $error = log_{10}(Bw_{obs}) - log_{10}(Bw_{model})$. The color indicates the number of samples in each bin. The error bars represent the weighted mean and WRMSE. The errors are much smaller at low *L* shells (<2.8) and gradually increase at high *L* shells, reflecting the highly fluctuating chorus wave amplitudes at large *L* shells. This is because the satellites are inside the plasmasphere at low L shells, where chorus waves are largely absent (see Figure 1f). As a result, the observations and model predictions are close to background noise, which results in small errors and bias. At higher *L* shells outside the plasmasphere, the variation of the wave amplitude from the noise level to the strong wave amplitude is large, resulting in a larger uncertainty. In the heart of the outer radiation belt (L~4-5), where chorus waves play an essential role in the acceleration and loss of the relativistic electrons, the uncertainty is about 0.5 in $log_{10}(Bw)$, which translates to an uncertainty of a factor of 3.0 (=$10^{0.5}$) in *Bw*.

Figure 4 shows the probability density of the errors as a function of the electron density for the four datasets. The error indicates the number of samples in each bin. The error bars represent the weighted mean and WRMSE. The errors are much smaller in high-density regions and suddenly become larger in low-density regions. At the density of $10^{1.8}$ cm^{-3}, which marks the plasmapause, there is a sharp transition in the model error. This is consistent with the sharp transition of $10^{1.8}$ cm^{-3} in Figure 2, where the chorus waves are mainly observed at low-density regions. As discussed above, this is because chorus waves are observed outside the plasmapause, thus resulting in quiet background noise inside the plasmapause and highly fluctuating chorus amplitude outside the plasmapause.

5 Model application

For illustration purposes, the chorus model was applied to a three-day period over October 24-27, 2017, which was held out as an out-of-sample test dataset. Therefore, this case can represent the forecast capability of the chorus model on out-of-sample datasets, and the results are shown in Figure 5.

The geomagnetic activity was quiet before 0800 UT on October 24, when a corotating interaction region (CIR) arrived at the Earth's magnetopause. The solar wind speed increased from 400 km/s to 650 km/s during the next two days, with a leading pressure enhancement between 0800-1200 UT on October 24 (not shown). The CIR induced a two-day activity period, which is similar to, but too weak to account for a geomagnetic storm. The Sym-H index in Figure 5a shows a sudden commencement between 0800-1200 UT on October 24, then reached a minimum of -36 nT around 2300 UT. Many magnetospheric substorms occurred subsequently, with two strong substorms reaching more than 1100 nT in the AE index during the storm's main phase. Another weak storm with a minimum Sym-H of -44 nT occurred on October 26.

Figures 5b and 5c show the comparison between the observed (red) and model-predicted (blue) LB chorus wave amplitude along the trajectories of the Van Allen Probes (RBSP-A and RBSP-B), the apogees of which were on the dayside. The chorus model predicts the chorus wave amplitude well along the trajectories, as the lines are very close. During the first orbit with no chorus waves, the model predicted background values. During the successive few orbits, the model predicted wave amplitude followed the trend of the observed value. For the first time, a chorus model can predict the peak amplitude of the strong chorus wave (~100 pT) during every orbit, including those of the second storm. In addition, the uncertainty of the model predictions is provided by the uncertainty model described in section 3.3. The model uncertainties (green lines) are larger for strong chorus waves and smaller for quiet times. For strong chorus waves, the model uncertainties are roughly 0.3, which translates to a factor of 2 ($10^{0.3}$). For quiet times, the model uncertainties are roughly 0.1, translating to a factor of 1.2.

Figure 5d shows the model-predicted chorus wave amplitude on the equatorial plane near midnight (MLAT=0° and MLT=3). First, the chorus wave enhancements are closely related to the substorm activity indicated by the SME index. For example, the chorus waves strengthened during the first two strong substorms in the storm main phase. Second, the chorus wave amplitude extended to lower *L* shells during strong substorms. This is because of the erosion of the plasmasphere due to the electric fields brought by the substorm injections. Thus, the chorus waves, excited right outside the plasmapause, also contracted to lower *L* shells [Hartley et al., 2022; Malaspina et al., 2016, 2018, 2020, 2021].

One of the merits of the neural network model is that it can reconstruct the global distribution of chorus wave amplitude at any time. The evolution of the chorus waves on the equatorial plane (MLAT=0°) is shown in Figure 6a. The arrows indicate the six snapshots in

Figure 5. There were no chorus waves during the quiet time at 2017-10-24/08:00:00. Right after the substorm onset at 2017-10-24/13:00:00, the chorus waves were strengthened at high L shells outside the nominal plasmapause indicated by the black line (n_e =50cm^{-3}). The wave amplitude is higher in the midnight and early morning region and lower toward noon. This distribution is consistent with the drift path of the injected electrons. At the peak of the first substorm at 2017-10-24/13:00:00, the chorus waves further strengthened and moved to the lower *L* shell as the plasmapause contracted. Nevertheless, the model-predicted chorus waves were outside the nominal plasmapause. At the peak of the second substorm at 2017-10-24/17:00:00, the chorus waves were stronger and reached lower *L* shell and broader local times. This is because the second substorm was stronger, and the plasmapause was more contracted. After the two substorms at 2017-10-24/20:30:00, the chorus waves were observed at higher *L* shells while the plasmapause remained contracted. During the second storm with an elevated SME index, similar to steady magnetospheric convection (Kissinger et al., 2012; McPherron et al., 2005; O'Brien et al., 2002; Sergeev et al., 1996), the chorus waves were stronger, extended to lower *L* shells, and broader local times.

The evolution of the chorus waves in the meridian plane is investigated in Figure 6 at four different MLTs (MLT=0, 3, 6, 9, and 12). Near midnight (MLT=0), the chorus waves peaked at the equator (MLAT=0°), and the amplitude decreased toward higher latitudes due to Landau damping of chorus waves (Bortnik et al., 2006). The chorus waves further strengthened and covered an extensive range of latitudes when the substorm strengthened. Nevertheless, the peak remained at the equator. In the dawn region (MLT=6), the chorus waves are strong and located at higher *L* shells, yet still near the equator. However, note that a minimum wave amplitude is found near the equator right outside the plasmapause, i.e., at the inner edge of the chorus wave region. The minimum in the wave amplitude is more pronounced toward the dayside, except in the plume region where the plasmapause extended to a large *L* shell. The equatorial minimum in chorus wave amplitude can be explained by two possible mechanisms: wave propagation and a local minimum in magnetic field strength, which is further elaborated on in the discussion section.

The temporal evolution of the chorus wave amplitudes versus MLAT at different L shells and MLT is illustrated in Figure 7. First, similar to Figure 5d, the chorus amplitude strengthens during substorms. Second, near the region of plasma injections (MLT=0), the chorus waves peak at the equator throughout this period, regardless of *L* shell and geomagnetic activity phases. On the other hand, toward the noon region, an equatorial minimum in wave amplitude was evident at different *L* shells during this period. Figure 7 further validates the equatorial minimum near the noon region during different activity and *L* shells, as shown in Figure 6.

The comparison between the IR chorus model and the traditional neural network model in Figure 8 further demonstrates the importance of imbalanced regression. A traditional neural network (NN) of the LB chorus amplitude is trained with an MSE loss function, which does not consider the weights of the imbalanced dataset. The IR chorus model and the traditional NN model are applied to the Van Allen Probe era (January 1, 2013 to June 1, 2019). The IR chorus model (Figure 8c) shows good agreement with the observed chorus amplitude from both Van Allen Probes (Figure 8b). Note that the IR chorus model could predict the strong chorus waves $10^{2.5}$ pT (300 pT). On the other hand, the traditional NN model (Figure 8d) is capped at about $10^{1.5}$ pT (30 pT) and cannot predict strong chorus waves. Therefore, the traditional NN model underestimates the strong chorus wave amplitude by a factor of 10. Furthermore, both models are applied to the equatorial plane (MLAT=0°) at MLT=0300 throughout the Van Allen Probe era.

The IR chorus model predicted many strong chorus wave events (red events in Figure 8e), while the traditional NN severely underestimated the wave amplitudes (green color in Figure 8f). Figures 8g and 8h show the zoomed-in view of the comparison during October 24-27, 2017, the same time period as Figure 5. Note that the chorus waves were strong (~100 pT) during this period, both in observations (Figure 5) and the IR model reconstructions (Figure 8g). However, the traditional NN model underestimated the chorus wave amplitude and predicted the yellow color at peaks rather than the red color from the IR chorus models, which is roughly a factor of 10 smaller. In summary, the IR chorus model can predict the strong amplitude of strong chorus waves with an uncertainty of a factor of 3. On the other hand, the traditional model underestimates these waves by a factor of 10.

5 Discussion and Conclusions

We develop a neural network-based model of the LB chorus wave amplitude in the inner magnetosphere. The model uses a combination of the satellite location, in-situ plasma density, and time series of the SME index as input and predicts the LB chorus wave amplitude in the inner magnetosphere ($L \leq 7$ and $|MLAT| < 20°$). The model is trained using 7-year observations (2013-2019) from the EMFISIS instrument onboard two Van Allen Probes. It was found that the auroral electrojet index SME alone can fully represent the geomagnetic activity related to the chorus waves. This is expected since the SME index indicates the strength of substorm injections, which induce electron anisotropy and load to the cyclotron resonant interactions. Furthermore, the neural network model can predict most of the chorus wave amplitude within an uncertainty of a factor of 2 and the chorus wave amplitude in the heart of the radiation belt (*L*~4-5) within an uncertainty of 1.6-2.1.

Using imbalanced regressive methods to develop the chorus waves model is essential because the database is highly imbalanced. About 90% of the observations are non-chorus samples ($Bw<3\ pT$), and only 5.6% of the data contains chorus waves ($Bw>10\ pT$). Traditional regression methods are usually dominated by non-chorus quiet data samples. As a result, traditional models tend to underestimate strong chorus waves, which are the most important and exciting to radiation belt physics. In this study, we utilized a loss function WMSE to account for different weighting factors for data samples of different chorus wave amplitudes. Our results demonstrate that this is a simple and effective way to deal with the imbalanced chorus wave dataset. As a result, our model can predict the large amplitude chorus waves in statistical analysis (Figure 2), event studies (Figure 5), and long-term predictions (Figure 8). Our study shows the importance of imbalanced regression in model development, both for machine learning models and traditional statistical models. Therefore, imbalanced regression (and classification) should be emphasized in the space physics/weather community since most datasets in our fields are highly imbalanced.

For the first time, the global temporal and spatial evolution of the chorus waves can now be investigated. Taking advantage of the neural networks' predictive capability, we can reconstruct the global distribution of chorus waves at a time instance within the coverage of the database ($L\leq7$ and $|MLAT|<20°$). The chorus waves are distributed in a region consistent with the injected electron drift path, which agrees with theoretical expectations. The chorus waves are typically distributed outside the nominal plasmapause regardless of MLT and levels of geomagnetic activity. As substorms develop, the chorus waves move to the lower *L* shells along with the erosion of the plasmapause, especially on the nightside. They also extend to a much broader region in MLT. On the other hand, the chorus waves in the noon-to-dusk region move to high L shells due to the formation of plasmaspheric plumes.

The latitudinal distributions of chorus waves show interesting evolutions. Chorus waves have their maximum amplitude near the equator and are confined to the plasma sheet region near midnight (MLT=3), which is close to the source MLT of the injections. During substorms, the amplitude and coverage of chorus waves can vary, expanding and contracting in MLT. Regardless, the chorus waves have peaks in the plasma sheet near midnight, where substorm injections are most frequent. Approaching the noon region, the chorus waves show a minimum at the equator, with peak amplitudes at higher latitudes in both hemispheres. This feature is consistent with statistical chorus wave distributions from multi-satellite observations (Meredith et al., 2021). Two possible explanations exist for the equatorial minimum in the chorus wave amplitude. First, chorus waves are excited near the equator, then propagate toward high latitudes and become more oblique (Bortnik et al., 2008, 2009, 2011; Chen et al., 2013). Thus, the chorus waves at higher latitudes at a specific L shell might originate from the equator at higher L shells. This means there is little chorus wave power near the equator at the same lower L shell, thus manifesting as a local equatorial minimum of chorus amplitude. This is consistent with a statistical study showing that the minimum near the equator on the dayside disappears at large *L* shells (Meredith et al., 2020), although beyond the range of the Van Allen Probes orbit (L~7). Thus, it also supports the first explanation that the waves are excited near the equator at higher *L* shells ($L>6$) and propagate to lower *L* shells at higher latitudes. Second, the magnetic field strength exhibits local minimums off the equator in the dayside region (Tsurutani & Smith, 1977; Keika et al., 2012). The substorm injections will drift along the magnetic field minimum, thus, following the bifurcation of the magnetic field lines to both hemispheres. In addition, the excitation of the chorus waves is in favor of smaller electron gyrofrequency (f_{ce}). Therefore, the excitation of the chorus waves on the dayside shows the feature of bifurcation, i.e., off-equator maximums of chorus amplitude in both hemispheres. A further investigation will be carried out to distinguish the two explanations, which require observations from higher latitudes and additional information on wave polarization properties, such as wave normal angle and Poynting flux.

The Earth's radiation belt belts, consisting primarily of energetic electrons and protons with energies from a few keV to several MeV, are particularly hazardous to spacecraft and astronauts. Thus, the specification and prediction of Earth's radiation environment have been an essential topic in space physics and space weather. To understand and predict radiation belt dynamics, the traditional approach involves the integration of the Fokker-Planck (FP) equations (e.g., Ma et al., 2017; Kellerman et al., 2021). However, it requires three-dimensional time-varying distributions of waves to calculate the diffusion coefficients. While chorus waves play an essential role in the acceleration of relativistic electrons, previous empirical chorus models are parameterized by geomagnetic activity and cannot provide such distributions. This is especially important during geomagnetic storms due to their underestimation of large-amplitude chorus waves. Therefore, the IR-based chorus model will address the problem by providing IR-based modeled chorus distributions, especially these storm-time strong chorus waves, to the FP simulation to better predict the radiation belt environment (Bortnik et al., 2018). In future studies, a comprehensive environment including waves and plasma conditions predicted by machine learning models will be used as input to the FP simulation for prediction purposes.

We summarize the major conclusions as follows:

1. We develop a neural network model of the lower-band chorus wave amplitude using imbalanced regressive methods.

2. Based on feature selection, the time series of the SME index can capture the variation of the lower-band chorus waves.

3. Our IR chorus model can correctly predict the amplitude of the strong chorus waves, for the first time. A pilot model is developed to provide the model uncertainties.

4. The IR chorus model can predict the strong wave amplitude (> 300 pT) with an uncertainty of a factor of 3. On the other hand, the traditional neural network model's

prediction is capped by 30 pT, persistently underestimating the amplitude of strong chorus waves by a factor of 10.

5. The equatorial evolution of the chorus waves is consistent with the electron drift path of substorm injections.

6. The chorus waves peak at the equator (plasma sheet) in the source MLT near midnight. They show a minimum at the equator toward noon, with two off-equator amplitude peaks in two hemispheres.

7. Imbalanced regression methods require more attention since most datasets in space physics, space weather, and real world are imbalanced.

Acknowledgments

XC would like to thank grant NASA ECIP 80NSSC19K0911, 80NSSC20K0196, 80NSSC22K1023, 80NSSC20K1325, 80NSSC23K0096, 80NSSC18K1227, and AFOSR YIP FA9550-23-1-0359. In addition, JB acknowledges support from the Defense Advanced Research Projects Agency under the Department of the Interior award D19AC00009. WL, XS, and QM acknowledge NASA grants 80NSSC19K0845, 80NSSC20K0698, as well as the NSF grant AGS-1847818. This work used Extreme Science and Engineering Discovery Environment (XSEDE) Bridges GPU at the PSC through allocation TG-PHY190033.

Open Research

The chorus wavs are analyzed using measurement from the EMFISIS instrument (Kletzing et al., 2013) available at emfisis.physics.uiowa.edu onboard Van Allen Probe mission (Mauk et al., 2013) available at rbspgway.jhuapl.edu. The solar wind parameters and geomagnetic indices are obtained from the OMNI dataset (Papitashvili et al., 2020) available at omniweb.gsfc.nasa.gov and SuperMAG (Gjerloev et al., 2010) available at https://supermag.jhuapl.edu/. The data set and models of the chorus wave are available (Chu et al., 2023) at https://doi.org/10.5281/zenodo.7894060. The neural network models are developed using the TensorFlow package, which is open-source (TensorFlow Developers, 2023) and available at www.tensorflow.org.

References

A. Al-Ghraibah, L. E. Boucheron and R. T. J. McAteer, A Study of Feature Selection of Magnetogram Complexity Features in an Imbalanced Solar Flare Prediction Dataset, 2015 IEEE International Conference on Data Mining Workshop (ICDMW), Atlantic City, NJ, USA, 2015, pp. 557-564, doi: 10.1109/ICDMW.2015.188.

Agapitov, O., Artemyev, A., Krasnoselskikh, V., Khotyaintsev, Y. V., Mourenas, D., Breuillard, H., Balikhin, M., and Rolland, G. (2013), Statistics of whistler-mode waves in the outer radiation belt: Cluster STAFF-SA measurements, J. Geophys. Res. Space Physics, 118, 3407– 3420, doi:10.1002/jgra.50312.

Agapitov, O. V., Artemyev, A. V., Mourenas, D., Mozer, F. S., & Krasnoselskikh, V. (2015). Empirical model of lower band chorus wave distribution in the outer radiation belt. Journal of Geophysical Research: Space Physics, 120, 10,425–10,442. https://doi.org/10.1002/2015JA021829

Agapitov, O., D. Mourenas, A. Artemyev, F. S. Mozer, J. W. Bonnell, V. Angelopoulos, V. Shastun, and V. Krasnoselskikh (2018), Spatial Extent and Temporal Correlation of Chorus and Hiss: Statistical Results From Multipoint THEMIS Observations, J. Geophys. Res., 123(10), 8317-8330, doi:10.1029/2018ja025725.

Akiba, T., Sano, S., Yanase, T., Ohta, T., & Koyama, M. (2019). *Optuna: A next-generation hyperparameter optimization framework. Paper presented in proceedings of the 25th ACM SIGKDD international conference on knowledge discovery & data mining (KDD' 19)* (pp. 2623– 2631): Association for Computing Machinery. https://doi.org/10.1145/3292500.3330701

Baker DN, Kanekal SG, Hoxie VC, et al. A long-lived relativistic electron storage ring embedded in Earth's outer Van Allen belt. Science. 2013;340(6129):186-190. doi:10.1126/science.1233518

Baker DN, Jaynes AN, Hoxie VC, et al. An impenetrable barrier to ultrarelativistic electrons in the Van Allen radiation belts. *Nature*. 2014, 515(7528):531-534. doi:10.1038/nature13956

Baker, D. N., et al. (2014b), Gradual diffusion and punctuated phase space density enhancements of highly relativistic electrons: Van Allen Probes observations, *Geophys. Res. Lett.*, *41*(5), 1351-1358, doi:10.1002/2013gl058942.

Baker, D. N., Hoxie, V., Zhao, H., Jaynes, A. N., Kanekal, S., Li, X., & Elkington, S. (2019). Multiyear measurements of radiation belt electrons: Acceleration, transport, and loss. *Journal of Geophysical Research: Space Physics*, 124, 2588– 2602. https://doi.org/10.1029/2018JA026259

Bergstra, J., Bardenet, R., Bengio, Y. & Kégl, B. (2011). Algorithms for Hyper-Parameter Optimization. Paper presented at the 25th Annual Conference on Neural Information Processing Systems (NIPS 2011), Granada, Spain. https://proceedings.mlr.press/v28/bergstra13.html

Bergstra, J., Yamins, D., & Cox, D. (2013). Making a science of model search: Hyperparameter optimization in hundreds of dimensions for vision architectures. In *Paper presented at the proceedings of the 30th international conference on machine learning, proceedings of machine learning research*. Retrieved from http://proceedings.mlr.press

Bortnik, J., and R. M. Thorne (2007), The dual role of ELF/VLF chorus waves in the acceleration and precipitation of radiation belt electrons, *Journal of Atmospheric and Solar-Terrestrial Physics*, *69*(3), 378-386, doi:10.1016/j.jastp.2006.05.030.

Bortnik, J., Thorne, R. M., and Meredith, N. P. (2007), Modeling the propagation characteristics of chorus using CRRES suprathermal electron fluxes, J. Geophys. Res., 112, A08204, doi:10.1029/2006JA012237.

Bortnik, J., Thorne, R. M., Meredith, N. P., and Santolik, O. (2007), Ray tracing of penetrating chorus and its implications for the radiation belts, Geophys. Res. Lett., 34, L15109, doi:10.1029/2007GL030040.

Bortnik, J., R. M. Thorne, and N. P. Meredith (2008), The unexpected origin of plasmaspheric hiss from discrete chorus emissions, Nature, 452(7183), 62-66, doi:10.1038/nature06741.

Bortnik, J., W. Li, R. M. Thorne, V. Angelopoulos, C. Cully, J. Bonnell, O. Le Contel, and A. Roux (2009), An Observation Linking the Origin of Plasmaspheric Hiss to Discrete Chorus Emissions, Science, 324(5928), 775-778, doi:DOI 10.1126/science.1171273.

Bortnik, J., Chen, L., Li, W., Thorne, R. M., and Horne, R. B. (2011), Modeling the evolution of chorus waves into plasmaspheric hiss, J. Geophys. Res., 116, A08221, doi:10.1029/2011JA016499.

Chen L., R. M. Thorne, W. Li, and J. Bortnik (2013), Modeling the wave normal distribution of chorus waves, J. Geophys. Res. Space Physics, 118, 1074–1088, doi:10.1029/2012JA018343.

Bortnik, J., Li, W., Thorne, R. M., & Angelopoulos, V. (2016). A unified approach to inner magnetospheric state prediction. *Journal of Geophysical Research: Space Physics*, **121**(3), 2423– 2430. https://doi.org/10.1002/2015ja021733

Bortnik, J., Chu, X., Ma, Q., Li, W., Zhang, X., Thorne, R. M., et al. (2018). Artificial neural networks for determining magnetospheric conditions. In E. Camporeale, S. Wing, & J. R. Johnson (Eds.), *Machine learning techniques for space weather* (pp. 279– 300). Elsevier. https://doi.org/10.1016/b978-0-12-811788-0.00011-1

Buda, M., Maki, A., and Mazurowski, M. A. A systematic study of the class imbalance problem in convolutional neural networks. Neural Networks, 106:249–259, 2018.

Bunch, N. L., M. Spasojevic, and Y. Y. Shprits (2011), On the latitudinal extent of chorus emissions as observed by the Polar Plasma Wave Instrument, *J. Geophys. Res.*, *116*, doi:Doi 10.1029/2010ja016181.

Burtis, W. J. & Helliwell, R. A. Magnetospheric chorus: occurrence patterns and normalized frequency. *Planet. Space Sci.* **24**, 1007 (1976).

Camporeale, E. (2019). The challenge of machine learning in Space Weather: Nowcasting and forecasting. Space Weather, 17, 1166– 1207. https://doi.org/10.1029/2018SW002061

Camporeale, E., Chu, X., Agapitov, O. V., & Bortnik, J. (2019). On the generation of probabilistic forecasts from deterministic models. Space Weather, 17, 455– 475. https://doi.org/10.1029/2018SW002026

Chakraborty, S., & Morley, S. K. (2020). Probabilistic prediction of geomagnetic storms and the Kp index. *Journal of Space Weather and Space Climate*, *10*. https://doi.org/10.1051/swsc/2020037

Chen, L. J., J. Bortnik, R. M. Thorne, R. B. Horne, and V. K. Jordanova (2009), Three-dimensional ray tracing of VLF waves in a magnetospheric environment containing a plasmaspheric plume, Geophys. Res. Lett., 36, doi:10.1029/2009gl040451.

Chu, X., McPherron, R. L., Hsu, T.-S., & Angelopoulos, V. (2015). Solar cycle dependence of substorm occurrence and duration: Implications for onset. *Journal of Geophysical Research: Space Physics*, **120**(4), 2808– 2818. https://doi.org/10.1002/2015ja021104

Chu, X. N., Bortnik, J., Li, W., Ma, Q., Angelopoulos, V., & Thorne, R. M. (2017a). Erosion and refilling of the plasmasphere during a geomagnetic storm modeled by a neural network. *Journal of Geophysical Research: Space Physics*, **122**(7), 7118– 7129. https://doi.org/10.1002/2017ja023948

Chu, X., Bortnik, J., Li, W., Ma, Q., Denton, R., Yue, C., et al. (2017b). A neural network model of three-dimensional dynamic electron density in the inner magnetosphere. *Journal of Geophysical Research: Space Physics*, **122**(9), 9183– 9197. https://doi.org/10.1002/2017ja024464

Chu, X., Ma, D., Bortnik, J., Tobiska, W. K., Cruz, A., Bouwer, S. D., et al. (2021). Relativistic electron model in the outer radiation belt using a neural network approach. *Space Weather*, 19, e2021SW002808. https://doi.org/10.1029/2021SW002808

Chu, X. (2023). Distribution and evolution of chorus waves modeled by a neural network: the importance of imbalanced regression (Version 0.1) [Data and Software]. https://doi.org/10.5281/zenodo.7894060

T. Dozat, "Incorporating Nesterov momentum into Adam", *Proc. ICLR*, pp. 1-4, 2016.

Gjerloev, J. W., R. A. Hoffman, S. Ohtani, J. Weygand, and R. Barnes, Response of the Auroral Electrojet Indices to Abrupt Southward IMF Turnings (2010), Annales Geophysicae, 28, 1167-1182 [Dataset]. (www.ann-geophys.net/28/1167/2010/angeo-28-1167-2010.pdf),

Guo, Y., Ni, B., Fu, S., Wang, D., Shprits, Y. Y., Zhelavskaya, I. S., et al. (2022). Identification of controlling geomagnetic and solar wind factors for magnetospheric chorus intensity using feature selection techniques. Journal of Geophysical Research: Space Physics, 127, e2021JA029926. https://doi.org/10.1029/2021JA029926

Hartley, D. P., Kletzing, C. A., Santolík, O., Chen, L. & Horne, R. B. Statistical properties of plasmaspheric hiss from Van Allen Probes observations. *J. Geophys. Res.: Space Phys.* **123**, 2605–2619 (2018).

Hartley, D. P., C. A. Kletzing, L. Chen, R. B. Horne, and O. Santolík (2019), Van Allen Probes Observations of Chorus Wave Vector Orientations: Implications for the Chorus-to-Hiss Mechanism, Geophys. Res. Lett., 46(5), 2337-2346, doi:10.1029/2019gl082111.

Hartley, D. P., Chen, L., Christopher, I. W., Kletzing, C. A., Santolik, O., Li, W., & Shi, R. (2022). The angular distribution of lower band chorus waves near plasmaspheric plumes. *Geophysical Research Letters*, 49, e2022GL098710. https://doi.org/10.1029/2022GL098710

Horne, R. B., and R. M. Thorne (1998), Potential waves for relativistic electron scattering and stochastic acceleration during magnetic storms, *Geophys. Res. Lett.*, *25*(15), 3011-3014, doi:Doi 10.1029/98gl01002.

Kasahara, S. et al. Pulsating aurora from electron scattering by chorus waves. *Nature* **554**, 337–340 (2018).

Katoh Y, Omura Y, Computer simulation of chorus wave generation in the Earth's inner magnetosphere, GRL 34, L03102 (2007). http://dx.doi.org/10.1029/2006GL028594

Keika, K., Spasojevic, M., Li, W., Bortnik, J., Miyoshi, Y., and Angelopoulos, V. (2012), PENGUIn/AGO and THEMIS conjugate observations of whistler mode chorus waves in the dayside uniform zone under steady solar wind and quiet geomagnetic conditions, J. Geophys. Res., 117, A07212, doi:10.1029/2012JA017708.

Kim, J.-H., Lee, D.-Y., Cho, J.-H., Shin, D.-K., Kim, K.-C., Li, W., and Kim, T. K. (2015), A prediction model for the global distribution of whistler chorus wave amplitude developed separately for two latitudinal zones. *J. Geophys. Res. Space Physics*, 120, 2819– 2837, doi: 10.1002/2014JA020900.

Kissinger, J., McPherron, R. L., Hsu, T.-S., and Angelopoulos, V. (2012), Diversion of plasma due to high pressure in the inner magnetosphere during steady magnetospheric convection, *J. Geophys. Res.*, 117, A05206, doi:10.1029/2012JA017579.

Kletzing, C. A., et al. (2013), The Electric and Magnetic Field Instrument Suite and Integrated Science (EMFISIS) on RBSP, *Space Sci. Rev.*, **179**, 127–181, [Dataset] doi:10.1007/s11214-013-9993-6.

Kuhn, M., & Johnson, K. (2013). *Applied predictive modeling*: Springer.

Kurth, W. S., S. De Pascuale, J. B. Faden, C. A. Kletzing, G. B. Hospodarsky, S. Thaller, and J. R. Wygant (2015), Electron densities inferred from plasma wave spectra obtained by the Waves instrument on Van Allen Probes, *J. Geophys. Res. Space Physics*, **120**, 904–914, doi:10.1002/2014JA020857.

Lazzús, J. A., Vega, P., Rojas, P., & Salfate, I. (2017). Forecasting the Dst index using a swarm-optimized neural network. *Space Weather*, *15*(8), 1068–1089. https://doi.org/10.1002/2017SW001608

Lee, D. Y., D. K. Shin, J. H. Kim, J. H. Cho, K. C. Kim, J. A. Hwang, D. L. Turner, T. K. Kim, and M. Y. Park (2013), Long-term loss and re-formation of the outer radiation belt, *J. Geophys. Res.*, *118*(6), 3297-3313, doi:10.1002/jgra.50357.

Li, W., R. M. Thorne, V. Angelopoulos, J. Bortnik, C. M. Cully, B. Ni, O. LeContel, A. Roux, U. Auster, and W. Magnes (2009), Global distribution of whistler-mode chorus waves observed on the THEMIS spacecraft, *Geophys. Res. Lett.*, *36*(9), L09104, doi:10.1029/2009gl037595.

Li W, Thorne RM, Nishimura Y, Bortnik J, Angelopoulos V, et al., THEMIS analysis of observed equatorial electron distributions responsible for the chorus excitation, JGR 115, A00F11 (2010). http://dx.doi.org/10.1029/2009JA014845

Li, W., J. Bortnik, R. M. Thorne, C. M. Cully, L. Chen, V. Angelopoulos, Y. Nishimura, J. B. Tao, J. W. Bonnell, and O. LeContel (2013), Characteristics of the Poynting flux and wave normal vectors of whistler-mode waves observed on THEMIS, *J. Geophys. Res. Space Physics*, **118**, 1461–1471, doi:10.1002/jgra.50176.

Li, W., Santolik, O., Bortnik, J., Thorne, R. M., Kletzing, C. A., Kurth, W. S., and Hospodarsky, G. B. (2016), New chorus wave properties near the equator from Van Allen Probes wave observations, *Geophys. Res. Lett.*, 43, 4725– 4735, doi:10.1002/2016GL068780.

Li, J., Bortnik, J., An, X. *et al.* Origin of two-band chorus in the radiation belt of Earth. *Nat Commun* **10**, 4672 (2019). https://doi.org/10.1038/s41467-019-12561-3

Li, X., D. N. Baker, M. Temerin, T. E. Cayton, E. G. D. Reeves, R. A. Christensen, J. B. Blake, M. D. Looper, R. Nakamura, and S. G. Kanekal (2013), Multisatellite observations of the outer zone electron variation during the November 3–4, 1993, magnetic storm, *Journal of Geophysical Research: Space Physics*, *102*(A7), 14123-14140, doi:10.1029/97ja01101.

Liu, Z., Miao, Z., Zhan, X., Wang, J., Gong, B., and Yu, S. X. Large-scale long-tailed recognition in an open world. In CVPR, 2019.

Ma, Q., Li, W., Bortnik, J., Thorne, R. M., Chu, X., Ozeke, L. G., et al. (2018). Quantitative evaluation of radial diffusion and local acceleration processes during GEM challenge events. *Journal of Geophysical Research: Space Physics*, 123, 1938– 1952. https://doi.org/10.1002/2017JA025114

Ma, D., Chu, X., Bortnik, J., Claudepierre, S. G., Tobiska, W. K., Cruz, A., et al. (2022). Modeling the dynamic variability of sub-relativistic outer radiation belt electron fluxes using machine learning. *Space Weather*, 20, e2022SW003079. https://doi-org.colorado.idm.oclc.org/10.1029/2022SW003079

Malaspina, D. M., Jaynes, A. N., Boulé, C., Bortnik, J., Thaller, S. A., Ergun, R. E., Kletzing, C. A., and Wygant, J. R. (2016), The Distribution of Plasmaspheric Hiss Wave Power with Respect to Plasmapause Location, *Geophys. Res. Lett.*, 43, 7878– 7886, doi:10.1002/2016GL069982.

Malaspina, D. M., Jean-Francois Ripoll, Xiangning Chu, George Hospodarsky, John Wygant, Variation in Plasmaspheric Hiss Wave Power With Plasma Density, Geophysical Research Letters, 10.1029/2018GL078564, **45**, 18, (9417-9426), (2018).

Malaspina, D. M., Hui Zhu, Alexander Y. Drozdov, A Wave Model and Diffusion Coefficients for Plasmaspheric Hiss Parameterized by Plasmapause Location, Journal of Geophysical Research: Space Physics, 10.1029/2019JA027415, **125**, 2, (2020).

Malaspina, D. M., Jaynes, A. N., Elkington, S., Chan, A., Hospodarsky, G., & Wygant, J. (2021). Testing the organization of lower-band whistler-mode chorus wave properties by plasmapause location. *Journal of Geophysical Research: Space Physics*, 126, e2020JA028458. https://doi.org/10.1029/2020JA028458

Mauk, B. H., Fox, N. J., Kanekal, S. G., Kessel, R. L., Sibeck, D. G., & Ukhorskiy, A. (2013). Science objectives and rationale for the radiation belt storm probes mission. *Space Science Reviews*, **179**(1–4), 3–27 [Dataset]. https://doi.org/10.1007/s11214-012-9908-y

McPherron, R. L., T. P. O'Brien, and S. M. Thompson (2005), Solar wind drivers for steady magnetospheric convection, in *Multiscale Coupling of the Sun-Earth Processes*, edited by A. T. Y. Liu, Y. Kamide, and G. Consolini, pp. 113–124, Elsevier, Amsterdam, doi:10.1016/B978-044451881-1/50009-5.

Meredith, N. P., R. B. Horne, and R. R. Anderson (2001), Substorm dependence of chorus amplitudes: Implications for the acceleration of electrons to relativistic energies, *J. Geophys. Res.*, *106*(A7), 13165-13178, doi:10.1029/2000ja900156.

Meredith, N. P., R. B. Horne, R. M. Thorne, and R. R. Anderson (2003a), Favored regions for chorus-driven electron acceleration to relativistic energies in the Earth's outer radiation belt, *Geophys. Res. Lett.*, *30*(16), 1871, doi:10.1029/2003gl017698.

Meredith, N. P., R. M. Thorne, R. B. Horne, D. Summers, B. J. Fraser, and R. R. Anderson (2003b), Statistical analysis of relativistic electron energies for cyclotron resonance with EMIC waves observed on CRRES, J. Geophys. Res., 108(A6), doi:10.1029/2002ja009700.

Meredith, N. P., Horne, R. B., Thorne, R. M., Summers, D., and Anderson, R. R. (2004), Substorm dependence of plasmaspheric hiss, J. Geophys. Res., 109, A06209, doi:10.1029/2004JA010387.

Meredith, N. P., R. B. Horne, A. Sicard-Piet, D. Boscher, K. H. Yearby, W. Li, and R. M. Thorne (2012), Global model of lower band and upper band chorus from multiple satellite observations, *J. Geophys. Res.*, *117*, doi:Doi 10.1029/2012ja017978.

Meredith, N. P., Horne, R. B., Kersten, T., Li, W., Bortnik, J., Sicard, A., et al. (2018). Global model of plasmaspheric hiss from multiple satellite observations. *Journal of Geophysical Research: Space Physics*, **123**(6), 4526–4541. https://doi.org/10.1029/2018JA025226

Meredith, N. P., Horne, R. B., Shen, X.-C., Li, W., & Bortnik, J. (2020). Global model of whistler mode chorus in the near-equatorial region. Geophysical Research Letters, 47(11) e2020GL087311. https://doi.org/10.1029/2020GL087311

Meredith, N. P., Bortnik, J., Horne, R. B., Li, W., & Shen, X.-C. (2021). Statistical investigation of the frequency dependence of the chorus source mechanism of plasmaspheric hiss. *Geophysical Research Letters*, 48, e2021GL092725. https://doi.org/10.1029/2021GL092725

Morley, S. K., Brito, T. V., & Welling, D. T. (2018). Measures of model performance based on the log accuracy ratio. Space Weather, 16, 69– 88. https://doi.org/10.1002/2017SW001669

Ni, B., Thorne, R. M., Shprits, Y. Y. & Bortnik, J. Resonant scattering of plasma sheet electrons by whistler-mode chorus: contribution to diffuse auroral precipitation. *Geophys. Res. Lett.* **35**, L11106 (2008).

Ni, B. B., J. Bortnik, R. M. Thorne, Q. L. Ma, and L. J. Chen (2013), Resonant scattering and resultant pitch angle evolution of relativistic electrons by plasmaspheric hiss, *J. Geophys. Res.*, *118*(12), 7740-7751, doi:10.1002/2013ja019260.

Ni, B. et al. Origins of the Earth's diffuse auroral precipitation. *Space Sci. Rev.* **200**, 205–259 (2016).

Nishimura, Y. et al. Identifying the driver of pulsating aurora. *Science* **330**, 81–84 (2010).
Kasahara, S. et al. Pulsating aurora from electron scattering by chorus waves. *Nature* **554**, 337–340 (2018).

Nishizuka, N., Kubo, Y., Sugiura, K. *et al.* Operational solar flare prediction model using Deep Flare Net. *Earth Planets Space* **73**, 64 (2021). https://doi.org/10.1186/s40623-021-01381-9

Nunn, D., A self-consistent theory of triggered VLF emissions, P&SS 22, 349-378 (1974). http://dx.doi.org/10.1016/0032-0633(74)90070-1

O'Brien, T. P., S. M. Thompson, and R. L. McPherron (2002), Steady magnetospheric convection: Statistical signatures in the solar wind and AE, *Geophys. Res. Lett.*, **29**(7), 1130,

Omura Y, Katoh Y, Summers D, Theory and simulation of the generation of whistler-mode chorus, JGR 113, A04223, (2008). http://dx.doi.org/10.1029/2007JA012622

Papitashvili, Natalia E. and King, Joseph H. (2020), "OMNI 1-min Data", NASA Space Physics Data Facility [Dataset], https://doi.org/10.48322/45bb-8792

Reeves, G. D., K. L. McAdams, R. H. W. Friedel, and T. P. O'Brien (2003), Acceleration and loss of relativistic electrons during geomagnetic storms, *Geophys. Res. Lett.*, *30*(10), 1529, doi:10.1029/2002gl016513.

Reeves, G. D., et al. (2013), Electron acceleration in the heart of the Van Allen radiation belts, *Science*, *341*(6149), 991-994, doi:10.1126/science.1237743.

Rothe, R., Timofte, R., and Gool, L. V. Deep expectation of real and apparent age from a single image without facial landmarks. International Journal of Computer Vision, 126(2-4):144–157, 2018.

Santolík, O., Gurnett, D. A., Pickett, J. S., Parrot, M. & Cornilleau-Wehrlin, N. Spatio temporal structure of storm-time chorus. *J. Geophys. Res.* **108**(A7), 1278 (2003).

Sergeev, V.A., Pellinen, R.J. & Pulkkinen, T.I. Steady magnetospheric convection: A review of recent results. Space Sci Rev 75, 551–604 (1996). https://doi-org.colorado.idm.oclc.org/10.1007/BF00833344

Shen, X.-C., Li, W., Ma, Q., Agapitov, O., & Nishimura, Y. (2019). Statistical analysis of transverse size of lower band chorus waves using simultaneous multisatellite observations. *Geophysical Research Letters*, 46, 5725– 5734. https://doi.org/10.1029/2019GL083118

Srivastava, N., Hinton, G., Krizhevsky, A., Sutskever, I., & Salakhutdinov, R. (2014). Dropout: A simple way to prevent neural networks from overfitting. *Journal of Machine Learning Research*, **15**, 1929– 1958. http://jmlr.org/papers/v15/srivastava14a.html

Summers, D., C. Ma, N. Meredith, R. Horne, R. Thorne, D. Heynderickx, and R. Anderson (2002), model of the energization of outer-zone electrons by whistler-mode chorus during the October 9, 1990 geomagnetic storm, *Geophys. Res. Lett.*, *29*(24).

Tan, Y., Hu, Q., Wang, Z., & Zhong, Q. (2018). Geomagnetic Index Kp Forecasting With LSTM. *Space Weather*, *16*(4), 406–416. https://doi.org/10.1002/2017SW001764

Tang, K., Huang, J., and Zhang, H. Long-tailed classification by keeping the good and removing the bad momentum causal effect. In NeurIPS, 2020.

Temerin, M., and Li, X. (2002), A new model for the prediction of *Dst* on the basis of the solar wind, *J. Geophys. Res.*, 107(A12), 1472, doi:10.1029/2001JA007532, 2002

TensorFlow Developers. (2023). TensorFlow (v2.13.0-rc2) [Software]. Zenodo. https://doi.org/10.5281/zenodo.8071599

Thorne, R. M., Ni, B., Tao, X., Horne, R. B. & Meredith, N. P. Scattering by chorus waves as the dominant cause of diffuse auroral precipitation. *Nature* **467**, 943–946 (2010).

Thorne, R. M., et al. (2013a), evolution and slow decay of an unusual narrow ring of relativistic electrons near L similar to 3.2 following the September 2012 magnetic storm, *Geophys. Res. Lett.*, *40*(14), 3507-3511, doi:10.1002/grl.50627.

Thorne, R. M., et al. (2013b), Rapid local acceleration of relativistic radiation-belt electrons by magnetospheric chorus, *Nature*, *504*(7480), 411-414, doi:10.1038/nature12889.

Tsurutani, B. T. & Smith, E. J. Postmidnight chorus: a substorm phenomenon. J. Geophys. Res. 79, 118–127 (1974).

Tsurutani BT, Smith EJ, Two types of magnetospheric ELF chorus and their substorm dependences, JGR 82, 5112-5128 (1977). http://dx.doi.org/10.1029/JA082i032p05112

Wan, J., Fu, J.-F., Liu, J.-F., Shi, J.-K., Jin, C.-G., & Zhang, H.-P. (2021). Class imbalance problem in short-term solar flare prediction. *Research in Astronomy and Astrophysics*, *21*(9), 237. https://doi.org/10.1088/1674-4527/21/9/237

Wang, D., Shprits, Y. Y., Zhelavskaya, I. S., Agapitov, O. V., Drozdov, A. Y., & Aseev, N. A. (2019). Analytical chorus wave model derived from Van Allen Probe observations. Journal of Geophysical Research: Space Physics, 124, 1063– 1084. https://doi.org/10.1029/2018JA026183

Yang, Y., Zha, K., Chen, Y.-C., Wang, H., & Katabi, D. (2021). Delving into Deep Imbalanced Regression. arXiv preprint arXiv:2102.09554.

Zhao, H. et al. Plasmaspheric hiss waves generate a reversed energy spectrum of radiation belt electrons. *Nat. Phys.* **15**, 367 (2019).

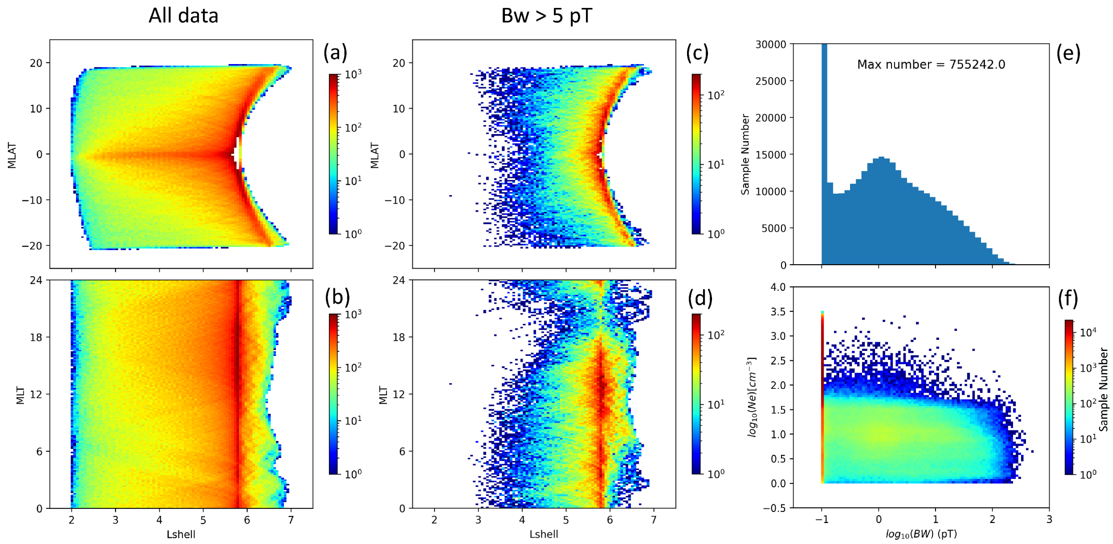

Figure 1. Statistical properties of the LB chorus wave amplitude $\log_{10}(B_w)$. The numbers of data samples as a function of (a) L shell and MLAT, (b) L shell and MLT, (e) wave amplitude, and (f) plasma density and wave amplitude. Panels (c) and (d) are in the same format as panels (a) and (b) but for Bw > 5 *pT*.

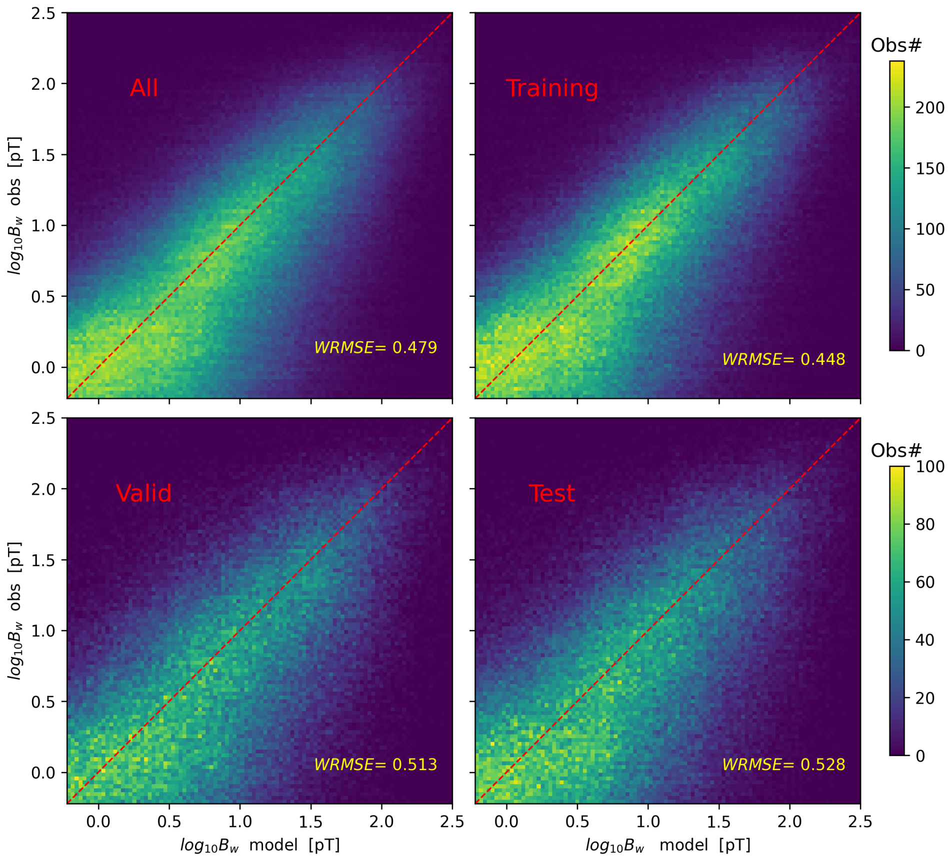

Figure 2. The two-dimensional distribution of the model predicted and observed LB chorus wave amplitude for four datasets (all, training, validation, and test). The red dashed lines are the diagonal line (y=x), indicating perfect agreement. The weighted root mean square errors (WRMSE) are shown on the bottom right of each panel.

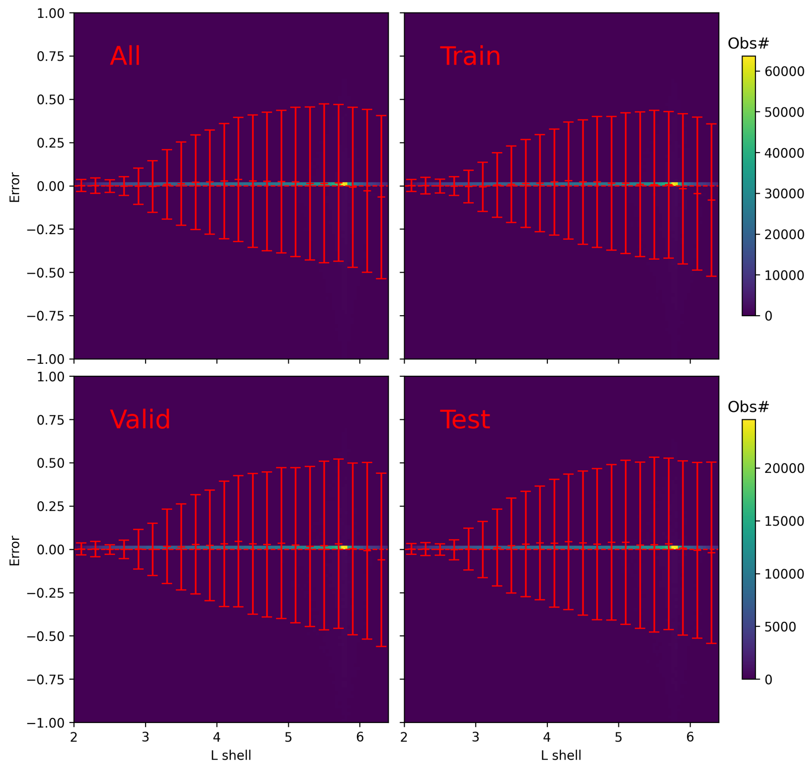

Figure 3. The error distribution as a function of the L shell for the four datasets (all, training, validation, and test). The error bars illustrate the weighted mean (marked by black crosses) and WRMSE.

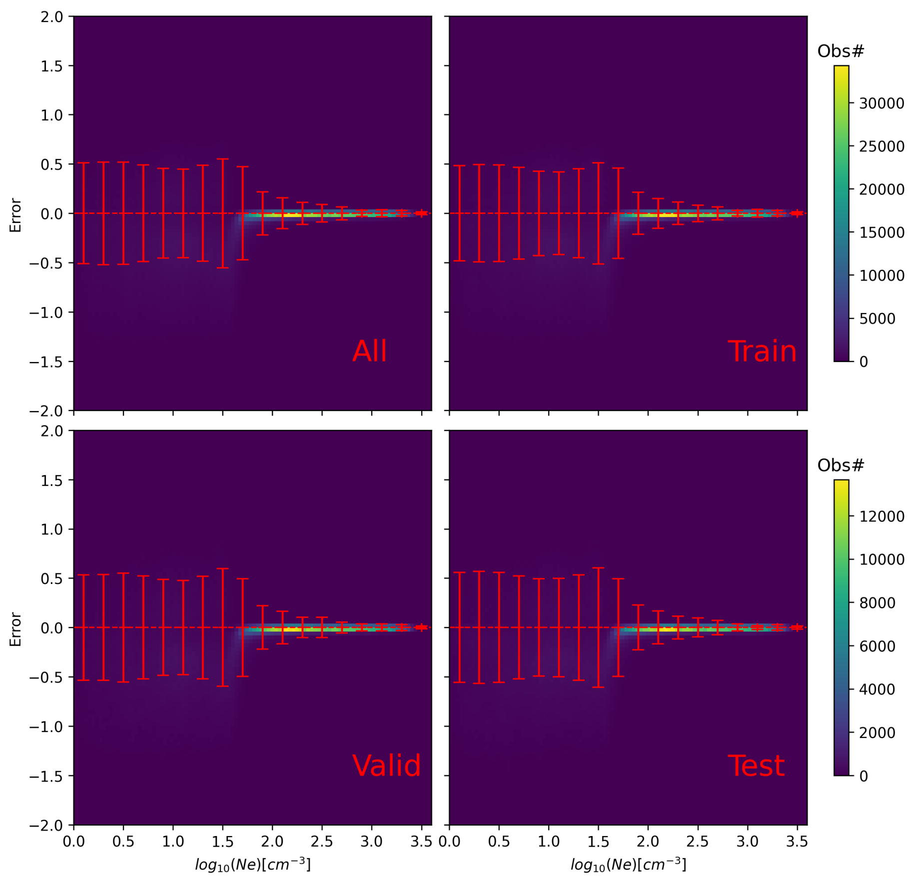

Figure 4. The error distribution as a function of the electron density for the four datasets (all, training, validation, and test). The error bars illustrate the weighted mean (marked by black crosses) and WRMSE.

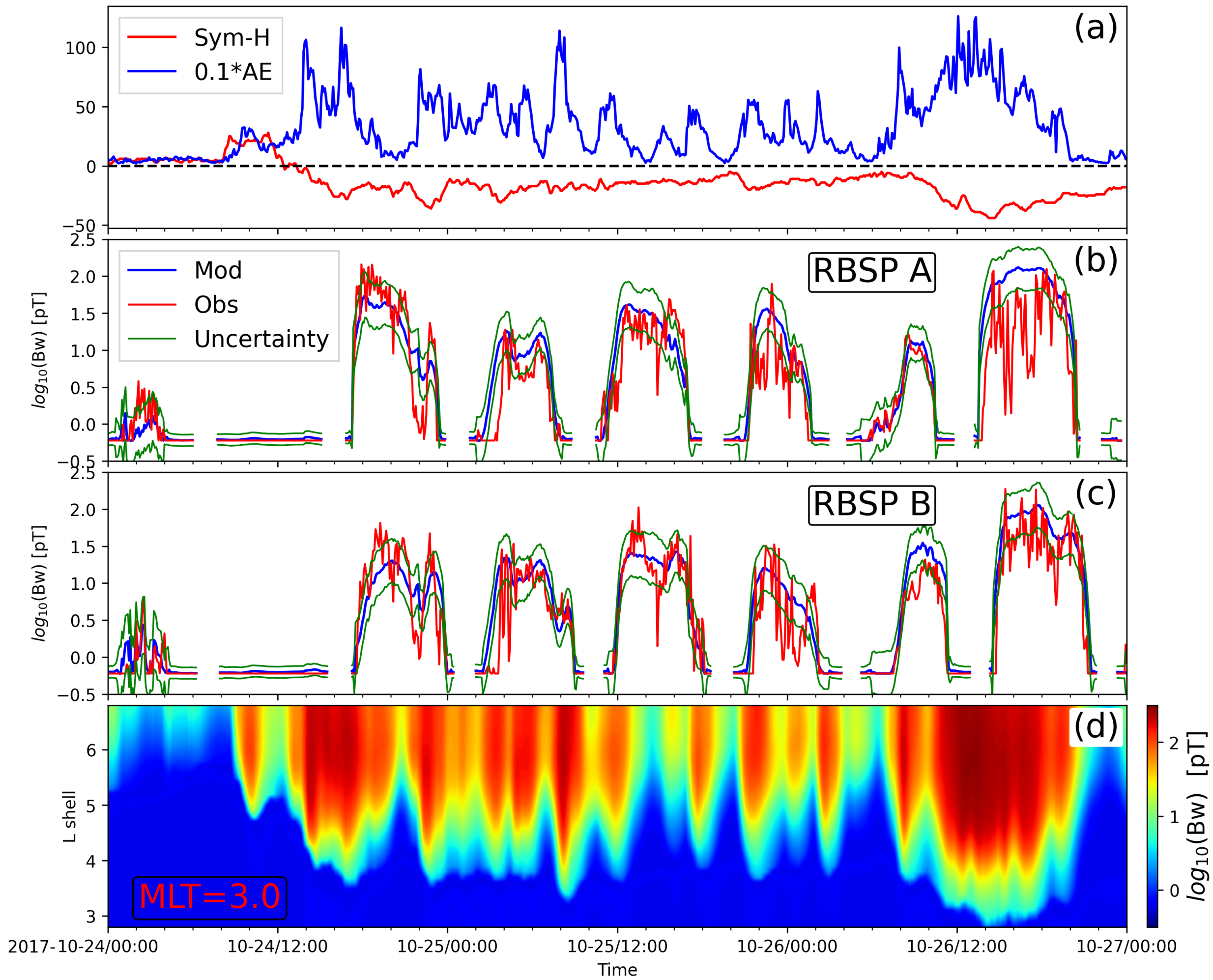

Figure 5. An application of the chorus model during a three-day period 24-27 October 2017, which is held out for test purposes. (a) Geomagnetic indices Sym-H and SME. (b-c) The comparison between the observed (red) and modeled (blue) LB chorus wave amplitude for Van Allen Probes (RBSP-A and RBSP-B). The green lines represent the model uncertainties. (d) The modeled LB chorus wave amplitude as a function of L shell on the equatorial plane (MLAT=0°) at MLT=0300. Note that the apogees of the Van Allen Probes were on the dayside (MLT~1200).

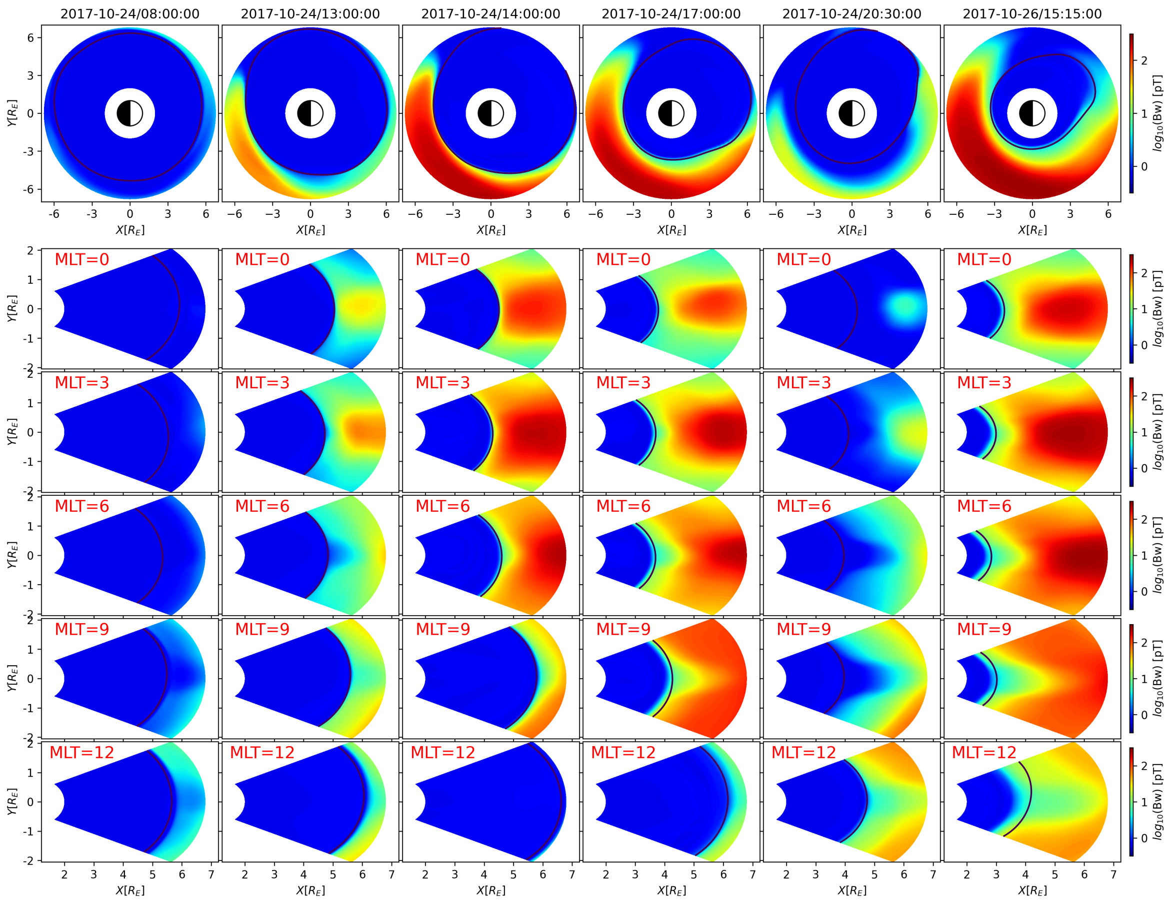

Figure 6. The evolution of chorus wave amplitude on the equatorial planes (top row) and meridian planes (bottom five rows) at different MLTs (MLT=0, 3, 6, 9, and 12).

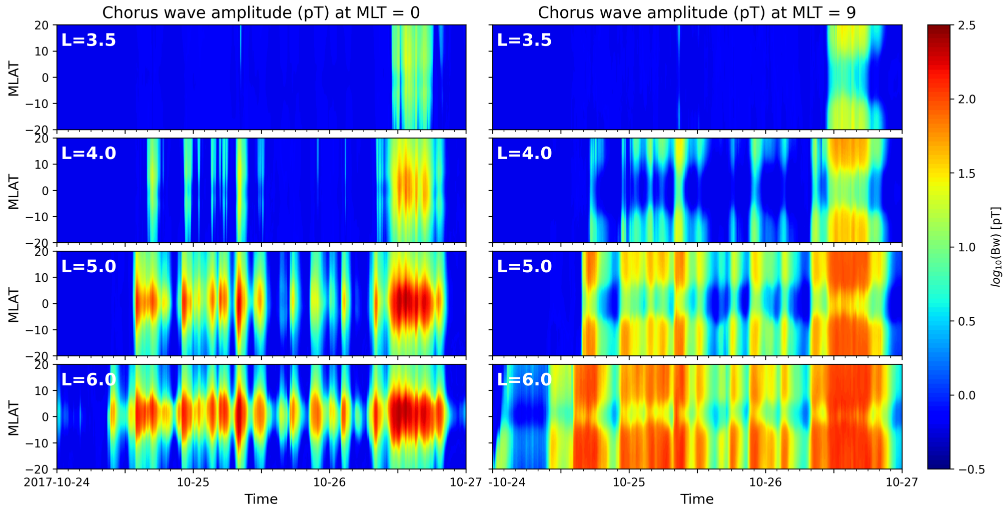

Figure 7. The temporal evolution of chorus wave amplitude as a function of MLAT at different L shells (L=3.5, 4.0, 5.0, and 6.0) near midnight (MLT=3, left) and near noon (MLT =9, right).

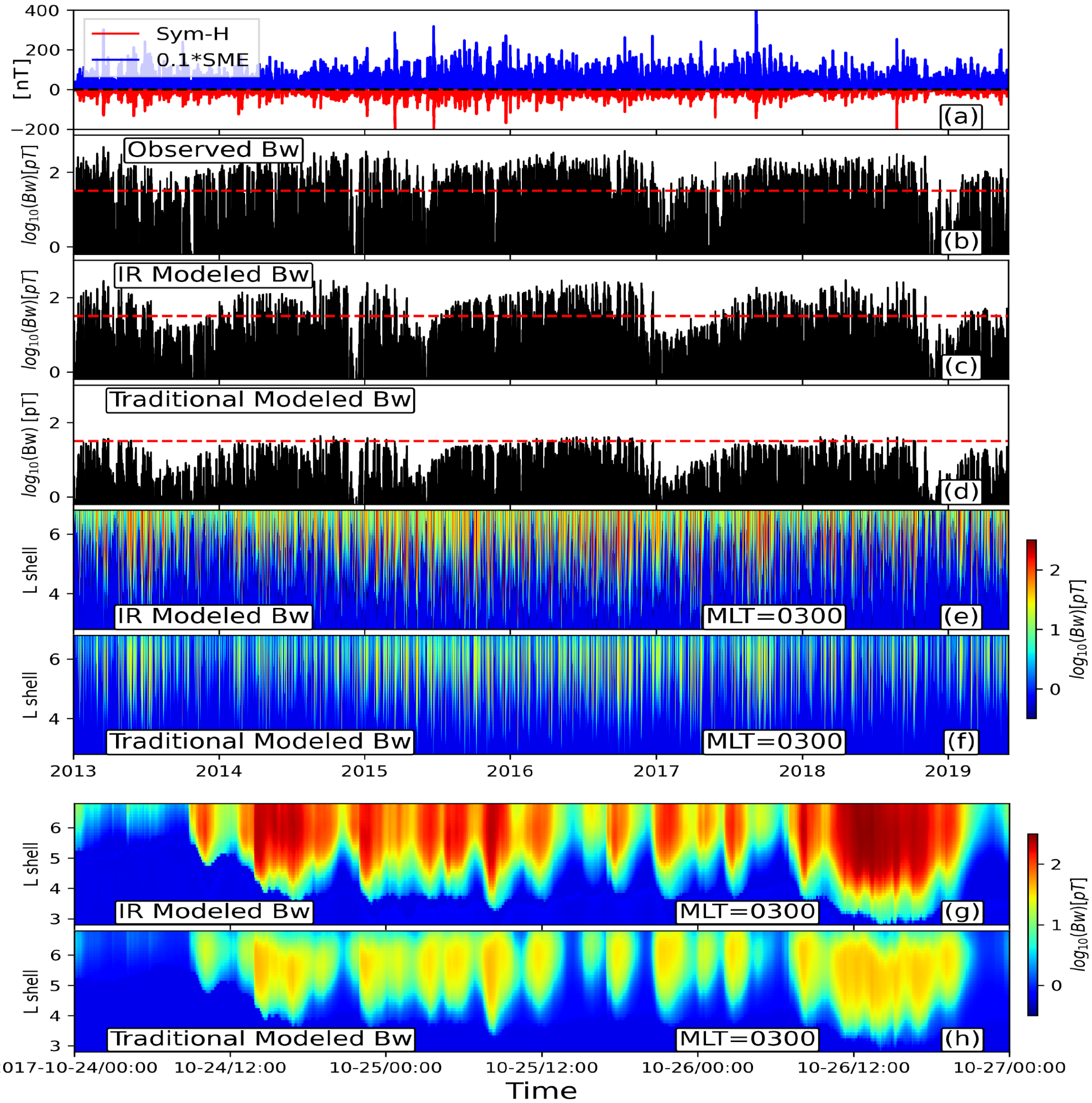

Figure 8. The comparison between the observed chorus amplitude and those modeled by the imbalanced regressive and traditional neural network (NN) models. (a) Geomagnetic indices Sym-H and SME, (b) the observed LB chorus wave amplitude along the trajectories of both Van Allen Probes; (c-d) the LB chorus wave amplitude modeled by imbalanced regressive NN model (c) and traditional NN model (d) along the trajectories of both Van

Allen Probes; (e-f) the LB chorus wave amplitude modeled by imbalanced regressive chorus model (e) and traditional NN model (f) on the equatorial plane (MLAT=0°) at MLT=0300. (g-h) Zoomed-in view of the LB chorus amplitude modeled by imbalanced regressive NN model (g) and traditional NN model (h) between October 24-27, 2017, the same period as Figure 5.